CrystEngComm

Data-Driven Deep Generative Design of Stable Spintronic Materials

Journal:	*CrystEngComm*
Manuscript ID	CE-ART-07-2023-000765.R2
Article Type:	Paper
Date Submitted by the Author:	15-Sep-2023
Complete List of Authors:	Siriwardane, Edirisuriya; University of Colombo, Physics Zhao, Yong; University of South Carolina, computer science Hu, Jianjun; University of South Carolina, ; Guizhou University,

DATA-DRIVEN DEEP GENERATIVE DESIGN OF STABLE SPINTRONIC MATERIALS

Edirisuriya M. Dilanga Siriwardane
Department of Physics
University of Colombo
Colombo 3, Sri Lanka

Yong Zhao
Department of Computer Science and Engineering
University of South Carolina
Columbia, SC 29201

Jianjun Hu *
Department of Computer Science and Engineering
University of South Carolina
Columbia, SC 29201
jianjunh@cse.sc.edu

September 15, 2023

ABSTRACT

Discovering novel magnetic materials is essential for advancing the spintronic technology with significant applications in data communication, data storage, quantum computing, and etc. While Density functional theory (DFT) has been widely used for designing materials, its high computational demand for estimating the magnetic ground states of even a single material limits its ability to explore the vast chemical design space for finding the right materials for spintronic applications. In this work, we developed a computational framework combining generative adversarial networks (GAN), machine learning (ML) classifiers, and DFT for de novo magnetic material discovery. We used the CubicGAN generative crystal structure design model for creating new ternary cubic structures. Machine learning classifiers were developed with around 90% accuracy to screen candidate ternary magnetic materials, which are then subject to DFT based stability validation. Our calculations discovered and confirmed that Na_6TcO_6, K_6TcO_6, and $BaCuF_6$ are stable ferromagnetic compounds, while Rb_6IrO_6 is a stable antiferromagnetic material. All those materials have zero energy above hull. Moreover, Na_6TcO_6 and $BaCuF_6$ are found to be half metals that are highly favorable for spintronic applications. Due to the structural differences, A_6MO_6 materials have a higher thermal capacity (C_v) compared to $BaCuF_6$. At 300 K temperature, C_v of A_6MO_6 materials is around 1100 $JK^{-1}mol^{-1}$ and that of $BaCuF_6$ is about 176 $JK^{-1}mol^{-1}$. This work demonstrates the promising potential of deep generative design for discovering novel functional materials.

Keywords Generative design · Deep learning · DFT · Magnetic materials · Material discovery · Spintronics

1 Introduction

Spintronic (spin-based electronics) technology has recently emerged by incorporating the spin degree of freedom into conventional charge-based electronics, as spintronic devices offer low power consumption and limited current leakage. Spintronics is considered for a vast amount of applications like energy harvesting, spin photovoltaics, and data storage [1]. In magnetic materials, the spin-polarized current is readily available due to different populations of spin-up and spin-down electrons [2, 3]. Therefore, magnetic materials are highly favorable for spintronic devices since their spin orientation can be efficiently manipulated using an external magnetic field. Spintronic devices like magnetic field sensors and hard-disk read-heads use giant-magneto resistance (GMR) to control the electron conductivity by aligning the spin direction of two ferromagnetic materials parallel or antiparallel to each other. GMR technology is widely used in the automotive industry, mobile phones, and the medical field [4, 5]. Lately, antiferromagnetic materials have

become attractive candidates for magnetic memories due to their benefits over ferromagnetic compounds, like their good stability under external magnetic fields, their capability of generating large magnetotransport effects, and the absence of stray fields [6, 7]. Therefore, both ferromagnetic and antiferromagnetic materials are vital for developing next-generation spintronic applications.

Designing computational methods for discovering novel ferromagnetic and antiferromagnetic materials is beneficial for the evolution of spintronic technology. Density functional theory (DFT) is widely utilized to discover novel materials and compounds [8, 9, 10, 11, 12, 13, 14]. DFT can be used to identify the potential magnetic materials [15, 16, 17, 18, 19, 20]. It is required to compare the DFT energies of nonmagnetic (NM), ferromagnetic (FM), and antiferromagnetic (AFM) states of a structure to locate the true magnetic ground state. One of the challenges of using DFT for the above purpose is the availability of multiple AFM configurations for a single compound. Thus, analyzing a large number of materials using DFT to find suitable candidates for spintronic applications is challenging. To reduce the computational burden, we are interested in informatics-guided approaches along with DFT for designing novel spintronic materials. Xia et al. predicted Fe_3CoB_2 magnetic compound employing machine learning (ML)–guided adaptive feedback method with DFT, and also they synthesized it using a conventional arc-melting process [21]. ML models were also developed by Long et al. [22] for intermetallic compounds to classify the AFM and FM materials and predict their Curie temperatures. Lu et al. developed an adaptive ML framework to search the chemical space with over 2×10^5 candidates to realize new 2-dimensional magnetic compositions [23]. However, it should be noted that most of those available machine learning techniques predict only the magnetic properties and compositions. They are not capable of predicting the compositions along with their structures.

The lack of ML models for discovering stable spintronic material structures motivated us to propose a new framework. In the computational material science field, structure prediction is one of the key problems. Recent studies [24] have shown that deep learning based generative models can be used to generate new stable crystal structures. In materials informatics, two types of generative models can be trained to generate crystal structures: Variational Autoencoders (VAEs) and Generative Adversarial Networks (GANs). A VAE model contains an encoder and a decoder: the encoder learns to represent materials with latent vectors and the decoder reconstructs the materials via latent vectors. After training, the decoder can be used to sample new materials. iMatGen [25] is the first work that uses VAEs to generate metastable V_xO_y materials. Later works [26, 27] use VAEs generate different types of materials with variations of VAEs' architectures. Like iMatGen, they have difficulty in generating high-symmetry materials because the VAEs do not have symmetry information in their training. On the other hand, A GAN also has two parts: a generator and a discriminator. The generator takes random noise as input to generate fake samples and the discriminator tells fake samples from real ones. CubicGAN [24] and PGCGM [28] are two typical crystal generative models using GANs. Both are provided with the space group in the training and physical losses are added in PGCGM to improve the performance. With symmetry information and physical losses, both can generate stable materials.

In this research, our design strategies for stable spintronic materials can be divided into four primary sections.

- **Chemical space:** Most probable combinations of elements for transition metal elements-based spintronics materials; Feature Importance of nonmagnetic-magnetic classifiers.
- **Structure:** Material generation using generative adversarial networks (GAN)
- **Magnetic Ground State:** Nonmagnetic-magnetic classifier development; the magnetic ground state verification using DFT.
- **Stability and Properties:** The thermodynamic, mechanical, and dynamical stability and the property investigation using DFT

First, we filter out the potential magnetic materials using information-guided approaches to lower the time consumption of the DFT calculations. Our chemical space analysis shows that the ternary transition metal element-based oxides and fluorides exhibit a higher probability of having a magnetic ground state. Furthermore, we developed a highly accurate deep neural network (DNN) and random forest classifier (RFC) to scan magnetic materials from the ternary cubic structures generated by the CubicGAN model. Feature Importance of the RFC model shows that a number of unfilled orbitals, availability of unfilled D and F orbitals, and the ground state magnetic moments of the elements play a significant role in classifying the nonmagnetic or magnetic compounds. From the predicted magnetic compounds, the DFT calculations encountered three stable transition metal elements-based oxides (Na_6TcO_6, K_6TcO_6, and Rb_6IrO_6) and one stable transition metal elements-based fluoride ($BaCuF_6$) with magnetic ground states. Thus, those three oxides have a common chemical formula type A_6MO_6. Here, Na_6TcO_6, K_6TcO_6, and $BaCuF_6$ exhibit ferromagnetic ground state while Rb_6IrO_6 has an antiferromagnetic ground state. Moreover, we found that $BaCuF_6$ and Na_6TcO_6 ferromagnetic materials are half-metals where only the spin-up bands can conduct. Due to the distinct structures in A_6MO_6 and $BaCuF_6$ materials, they contain considerably different physical properties. Our results show that A_6MO_6 materials ($Y > 50$ GPa and $G > 20$ GPa) have higher Young's (Y) and Shear (G) moduli compared to $BaCuF_6$

($Y < 13$ GPa and $G < 5$ GPa). On the contrary, $BaCuF_6$ has a higher Poisson's ratio (≈ 0.44) than that of the other three materials (< 0.25). The specific thermal capacity (C_v) of A_6MO_6 is much higher relative to $BaCuF_6$. At 300 K temperature, C_v of A_6MO_6 materials is approximately 1100 $JK^{-1}mol^{-1}$ and that of $BaCuF_6$ is around 176 $JK^{-1}mol^{-1}$.

2 Method

2.1 Generative design based on Generative Adversarial Network (GAN)

Generating crystal structures using generative models is a much harder task than generating images or text. Several unique challenges still remain that prevent generative models to generate materials under full spectrum of the periodic table: 1) The extreme variability, such as various number of elements/atoms in the crystal structure; 2) The generation of precise fractional coordinates and lattice parameters; 3) The extreme biased distribution of materials in 230 space groups; 4) The generation of materials with high symmetry.

The materials data used to discover potential stable magnetic materials is generated by our CubicGAN [24], which is a crystal generative model that can generate crystal structures for three cubic space groups at a large scale. CubicGAN tackles the crystal generative design challenges one by one via: 1) Nonequivalent atom positions are used to represent atoms' arrangement in unit cell. We chose ternary materials that have only nonequivalent atom positions (a.k.a, one element has one nonequivalent atom positions). In this way, the size of input data to the generative model can be same if we train a generator to generate only ternary materials. To obtain all atom positions in the unit cell, affine matrix is used to convert nonequivalent atom positions. Affine matrix is determined by space groups and it contains rotation and translation matrices. 2) Only cubic ternary materials are used to grain the generator. In this way, we only need to generate the length of cubic lattice. The angles are all $90°$. Then we discretize fractional coordinates by using fractional coordinate values in the set of $\{0.0, 0.25, 0.5, 0.75\}$. 3) We are not trying to generate crystal structures in 230 space groups like what VAE models claim [26, 29]. Instead, VAE models always generate crystal structures with very low symmetry [28]. On the other hand, we only use materials falling in three space groups of $Fm\bar{3}m$, $F\bar{4}3m$, and $Pm\bar{3}m$ because these three space groups are with greatest number of materials in OQMD [30] using selection criteria in CubicGAN.

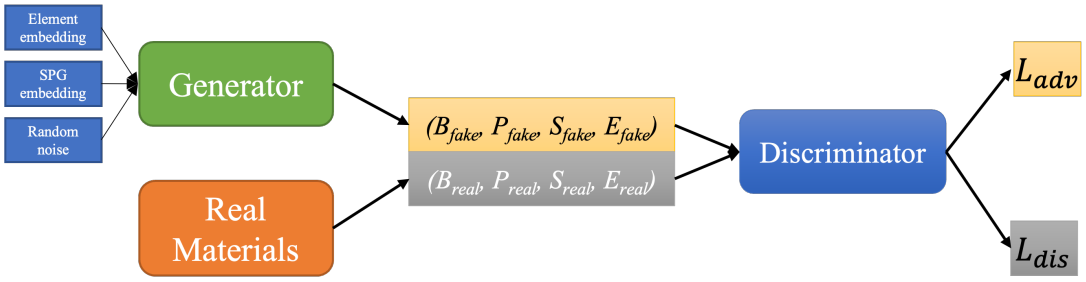

Figure 1: The framework of CubicGAN. It has two main learning components: generator and discriminator.

The main framework of CubicGAN is illustrated in Figure 1. The framework primarily contains two learning parts: generator and discriminator. The generator takes elements, space groups, and random noise as input and then generate three non-equivalent fractional coordinates B_{fake} and lattice parameters P_{fake} (only lengths since cubic structures have constant angles). With random chosen space group S_{fake} and Elements E_{fake}, we can assemble $M_{fake} = (B_{fake}, P_{fake}, S_{fake}, E_{fake})$ as the fake samples and the real samples $M_{real} = (B_{real}, P_{real}, S_{real}, E_{real})$ are collected through real crystal structures. Then discriminator learns to tell fake samples from real samples via two losses of L_{adv} and L_{dis} which are define below [31, 32]:

$$\begin{aligned} \hat{\mathcal{M}} &= \epsilon \mathcal{M}_{real} + (1-\epsilon)\mathcal{M}_{fake}, \quad \epsilon \sim U(0,1), \\ \mathcal{L}_{dis} &= D(\mathcal{M}_{fake}) - D(\mathcal{M}_{real}) + \lambda_d (\left\| \nabla_{\hat{\mathcal{M}}} D(\hat{\mathcal{M}}) \right\|_2 - 1)^2, \\ \mathcal{L}_{adv} &= -D(\mathcal{M}_{fake}), \end{aligned} \tag{1}$$

where $\hat{\mathcal{M}}$ is linearly interpolated between real samples $\mathcal{M}_{real}$ and fake samples $\mathcal{M}_{fake}$ and ϵ is uniformly sampled from 0 and 1. L_{adv} and L_{dis} are losses for training the generator and the discriminator. In L_{dis}, the penalty term

$(\left\|\nabla_{\hat{\mathcal{M}}} D(\hat{\mathcal{M}})\right\|_2 - 1)^2$ is used to help original Generative Adversarial Networks (GANs) stabilize and prevent GANs from collapsing to fixed mode because it enforces the norm of gradients to be close to 1. λ_d is set to 10 and $D(.)$ scores real and fake samples in the discriminator, respectively. The detailed architectures of generator and discriminator can be found in supplementary materials in CubicGAN [24].

After training, the generator generates (B_{gen}, P_{gen}) conditioning on (S_{gen}, E_{gen}) and then we assemble them into crystal structures. When 10 millions materials are generated, we find that most of the cubic materials in Materials Project and ICSD can be rediscovered. Then we filter down 10 millions by pymatgen CIFs readability, charge neutrality, and predicted negative formation energy for DFT relaxation. In final, 506 dynamically and mechanically stable ternary and quaternary new-prototyped materials are confirmed via phonon dispersion and mechanical property calculations.

2.2 Nonmagnetic-magnetic material Classifier

As we use the CubicGAN-generated ternary materials, we collected only the data of cubic ternary compositions from the material project (MP) database to develop nonmagnetic-magnetic classifiers. There were 10,285 materials in the above dataset, where 7,526 instances were nonmagnetic materials, while there were 2,759 magnetic compounds.

To develop the DNN and RFC models to classify the nonmagnetic and magnetic materials, we used 56 elemental and electronic structure attributes, such as total number of unfilled orbitals, atomic number, atomic weight, number of valence electrons, and number of unfilled s, p and d orbitals, to develop the feature set (see Supporting Information). Then, we computed the weighted average (Avg.) and the maximum difference of those properties for each chemical formula. The weighted Avg. of a property M of a ternary compound $\mathrm{A}_\alpha\mathrm{B}_\beta\mathrm{C}_\gamma$ was calculated based on the following expression,

$$M^{\mathrm{Avg}}_{\mathrm{A}_\alpha\mathrm{B}_\beta\mathrm{C}_\gamma} = \frac{1}{\alpha+\beta+\gamma}(\alpha M_{\mathrm{A}} + \beta M_{\mathrm{B}} + \gamma M_{\mathrm{C}}), \tag{2}$$

where M_{A}, M_{B} and M_{C} are the property M of A, B, amd C elements, respectively. Thus, we had 112 total number of features for the two classifiers.

Our deep neural networks (DNN) model was developed using Keras [33] on top of TensorFlow [34]. This model consists of two hidden layers where the first and second hidden layers include 56, and 28 neurons, respectively. The rectified linear unit (ReLu) activation function was included for each hidden layer of neurons to shift the summed weighted inputs. As the model is a classifier, the output layer was connected with the sigmoid activation function. We observed that randomly dropping out 50% of the units of the hidden layers helps to reduce the overfitting significantly. To reduce the overfitting further, we used Ridge (L2) regularization method for adding penalties during updating weights. As the optimizer, we employed the adaptive moment estimation (Adam) optimizer with a 0.0001 learning rate. The loss function and the metric of the DNN model were the binary cross-entropy for the training. Moreover, 500 epochs and 1500 batch sizes were included.

Our next machine learning model is a random forest classifier (RFC). An RFC is an ensemble classifier that builds multiple decision trees using a randomly chosen subset of the training dataset. Finally, unweighted voting from each decision tree is used to make predictions. The SearchCV algorithm in Scikit-learn program [35] was used to optimize the hyperparameters. The optimized number of decision trees, minimum samples split, minimum samples leaf, and maximum depth are 1000, 2, 1, and 80, respectively.

2.3 Density Functional Theory

We utilized the Vienna ab simulation package (VASP) code to perform the DFT calculations with the plane wave basis set where the cut-off energy was set as 500 eV [36, 37, 38, 39]. For the exchange-correlation potential, we considered the generalized gradient approximation (GGA) within the Perdew-Burke-Ernzerhof (PBE) formulation [40, 41]. The energy convergence criterion and the force convergence criterion were set to 10^{-8} eV and 10^{-2} eV/Å, respectively. The Brillouin zone integrations were carried out using a dense K-point mesh within the Monkhorst-Pack scheme. A $5\times5\times5$ K-mesh was used for the A_6MO_6 unit cells, while a $2\times5\times5$ K-mesh was used for their $2\times1\times1$ supercells. A $6\times6\times6$ K-mesh was used for the $BaCuF_6$ unit cells, while a $3\times6\times6$ K-mesh was used for their $2\times1\times1$ supercells. Since the considered cubic structures contain extensive lattice constants ($a > 8$Å) above K-meshes are sufficiently large. The density functional perturbation theory (DFPT) implemented in the VASP [42] program was used to determine the elastic constants. The bulk modulus (K), Shear modulus (G), Young's modulus (Y), and Poisson's ratio (ν) of the materials were calculated based on the Hill method using the VASPKIT code [43]. The phonon dissipation curves of the materials were obtained using Phonopy code [44]. We also carried out GGA+U [45, 46] calculations to determine whether the Hubbard parameter (U) affects the results. Those results are reported in the Supporting Information.

3 Results and Discussion

3.1 Probability of Discovering Transition Metal-based Spintronic Materials

One of the main objectives of this research is to find the most probable combinations of elements with transition metal elements for discovering spintronic materials. We first collected the composition, crystal system, and magnetic type of the ternary materials from the material project (MP) database. We considered the ternary materials with transition metal elements (M) and the common anions (X): O, F, N, S, Cl, Br, I, and H. We disregarded the rare-earth materials since we wanted the transition metal elements to be the source of the magnetism in the compounds. Only one of the above anions will appear in a single composition (i.e., if O is in a composition, then F, N, S, Cl, Br, I, or H is not present). Therefore, the chemical formulas take $A_\alpha M_\beta X\gamma$ form, where A can be any element type other than rare-earth or above anions.

In the MP database, we found 6,814 ferromagnetic, 872 antiferromagnetic, 2,382 ferrimagnetic, and 9,164 nonmagnetic ternary materials, which satisfy the above conditions. We regard all the ferromagnetic, antiferromagnetic, and ferrimagnetic compounds as magnetic/spintronics materials. Thus, altogether we have 10,068 magnetic and 9,164 nonmagnetic materials in the dataset. Next, we computed the probability of finding an $A_\alpha M_\beta X\gamma$ material for each X element as shown in Fig. 2. Since we specifically use CubicGAN to discover potential stable materials, cubic materials were also studied for the above anions. It is clear that O- and F-based $A_\alpha M_\beta X\gamma$ materials have a higher probability of being spintronic materials. When X=O or X=F, the probability of finding a magnetic material from all crystal systems is around 60 %, and it is less than 35 % for other anions. The dataset of cubic systems also shows that the $A_\alpha M_\beta O\gamma$ and $A_\alpha M_\beta F\gamma$ materials have a high probability of having a magnetic ground state. The probability of finding a cubic spintronics material is greater than 50 %, whereas that from other materials is less than 43 %. This indicates that one can focus on transition metal oxides and fluorides for discovering potential spintronics materials.

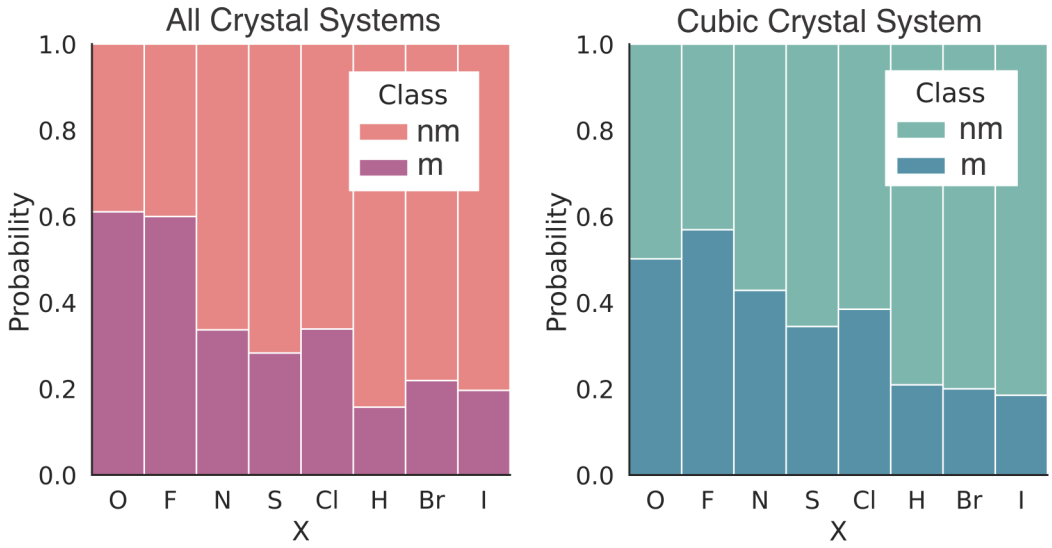

Figure 2: Probability of finding a ternary magnetic (m) and nonmagnetic (nm) material with transition metal elements and an anion (X).

3.2 Feature Importance

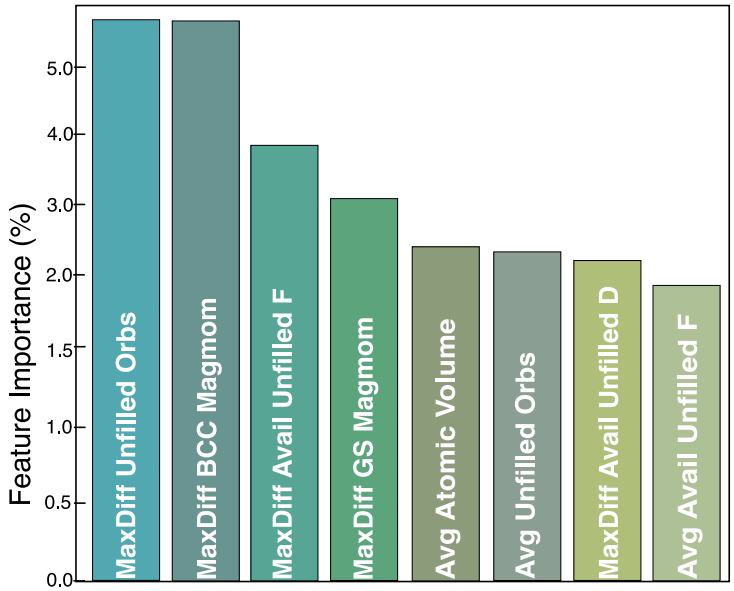

Figure 3: Feature Importance as a percentage ($> 1.8\%$) from the RFC model. Labels on the x-axis: Number of unfilled orbitals (Unfilled Orbs), magnetic moment of BCC structure of elements (BCC Magmom), availability of unfilled F orbitals (Avail Unfilled F), availability of unfilled D orbitals (Avail Unfilled D), and magnetic moment of ground state of elements (GS Magmom). MaxDiff, Avg and Avail, stand for the maximum difference of the feature, weighted average of the feature and availability, respectively.

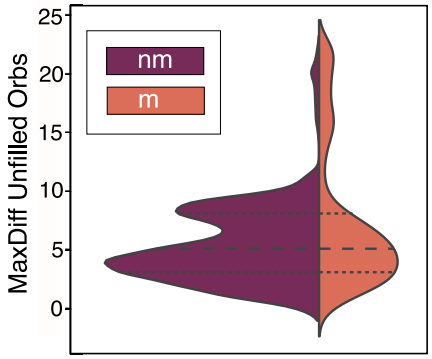

Figure 4: Number of ternary cubic magnetic (m) and nonmagnetic (nm) materials as a function of maximum difference of unfilled orbitals.

Feature Importance (FI) is a procedure that estimates a score for all the features of a given machine-learning model. The scores indicate the significance of each feature. A higher score means the specific feature will greatly impact the model used to predict a specific target. Figure 3 shows the RFC computed FI as percentages. Here, we show only the feature FI greater than 1.8 %. It is clear that the number of unfilled orbitals, availability of unfilled D and F orbitals, and the magnetic moments of the elements are the main influencing features of the RFC model to determine whether a material is magnetic or not. The number of unfilled orbitals is considerably higher in transition metal and rare earth elements. The magnetic moments of the ground state and BCC structure are nonzero for most of the materials formed with those elements (i.e., pure Fe, Co, and so on). The availability of unfilled D and F orbitals indicates the presence of partially filled D and F orbitals. Figure 4 shows the number of ternary cubic materials as a function of the maximum difference of unfilled orbitals for both nonmagnetic and magnetic classes. Based on our data, the nm: m ratio is 3.4:1 when the maximum difference of unfilled orbitals (MaxDiff Unfilled Orbs) is less than 11. If that quantity is greater

than 11, the nm:m ratio becomes 1:3.4. Thus, there is a higher probability of finding a magnetic material compared to nonmagnetic materials if MaxDiff Unfilled Orbs is greater than 11.

3.3 Predicting Potential Spintronics Materials

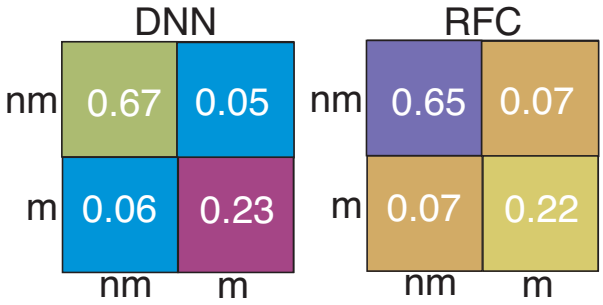

Figure 5: Confusion matrices of the DNN and RFC models for ternary cubic nonmagnetic (nm) and magnetic (m) material classification. The normalized values for true nm, true m, false nm and false m are mentioned.

Table 1: The classification report of the test set of nonmagnetic (nm) - magnetic (m) material classifiers.

	DNN			RFC			
	Precision	Recall	F1-score	Precision	Recall	F1-score	Support
nm	0.93	0.93	0.93	0.92	0.95	0.94	754
m	0.82	0.81	0.81	0.84	0.74	0.79	275
Accuracy			0.90			0.91	1029
Macro average	0.87	0.87	0.87	0.88	0.87	0.87	1029
Weighted average	0.90	0.90	0.90	0.90	0.90	0.90	1029

To train the DNN and RFC models, we randomly split the ternary cubic transition metal-based dataset into train and test subsets. The training subset contains 90 % of the 10,285 compositions, whereas the test subset has 10 %. The k-fold cross-validation is a technique utilized to assess the predicting ability of the model on new data. We used 3-fold cross-validation, which provides 0.885, 0.884, and 0.885 accuracies for each training step of DNN, while that of RFC are 0.915, 0.898, and 0.900. Thus, we got 0.88 ± 0.0005 and 0.90 ± 0.01 mean accuracy for the DNN and RFC models, respectively. Figure 5 shows the normalized confusion matrices of the two machine learning models. After classifying the materials, 67 (65) % were identified as nonmagnetic materials, and 23 (22) % were predicted as magnetic materials by the DNN (RFC) models correctly. The false nonmagnetic and false magnetic materials are less than 8 % from both models. In the test dataset, $\approx$ 28 % of the data were magnetic materials, and $\approx$ 72 % of them were nonmagnetic materials. Therefore, the true nonmagnetic and true magnetic data have a good agreement with the percentages in the test dataset.

The classification reports of the two machine learning models are given in Table 1. Precision indicates the quality of a positive prediction made by the model. Precision is given by the number of true positives divided by the total number of positive predictions. The DNN and RFC models exhibit 0.93 (0.82) and 0.92 (0.84) precision for the nonmagnetic (magnetic) materials, respectively. The recall is computed as the ratio between the number of positive samples accurately categorized as positive to the total number of Positive instances in the test dataset. The recall from the DNN model is 0.93 (0.81), and that from the RFC model is 0.93 (0.81) for the nonmagnetic (magnetic) compositions. The weighted average of precision and recall is given the F1-score, which is 0.93 (0.81) from the DNN model and 0.95 (0.74) from the RFC model for the nonmagnetic (magnetic) compositions. Finally, the accuracy of the models was calculated as the total number of correctly predicted samples over the total number of samples. It was found that the accuracy of the DNN model for the test set is 0.90 and that for the training set is 0.93. However, the accuracy of the RFC model is 0.91 for the test set and ≈ 1 for the train set. As a result of having an accuracy ≈ 1 for the training set, the RFC model can show poor performance on the new data samples. Therefore, we used the DNN model for predicting the new spintronic materials.

The CubicGAN model generated 183 mechanically and dynamically stable ternary cubic materials. However, only 141 compositions contain transition metal elements. Our DNN predicts that 45 of them are magnetic materials (See Supporting Information). Nevertheless, only four comply with all thermodynamic (negative formation energy and zero

energy-above hull), dynamical (no negative phonon frequencies), and mechanical stability criteria. Those materials are $BaCuF_6$, Na_6TcO_6, K_6TcO_6 and Rb_6IrO_6. Thus, three of them have the common chemical formula type, i.e., A_6MO_6.

3.4 Structure and Magnetic Properties

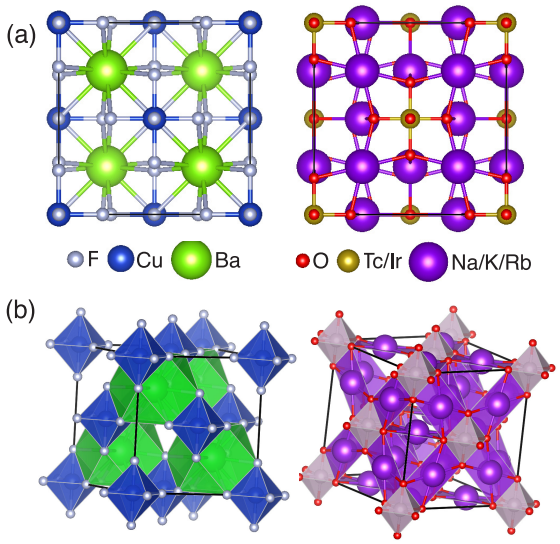

Figure 6: (a) Side views and (b) polyhedra of $BaCuF_6$ and A_6MO_6 materials.

$BaCuF_6$ material was found with the space group $F\bar{4}3m$ (216), while that of A_6MO_6 materials is $Fm\bar{3}m$ (225). Thus, both materials are face-centered cubic structures. The conventional unit cell of A_6MO_6 materials contains 52 atoms where 24 atoms are A, 4 atoms are M elements, and 24 atoms are O. However, the conventional unit cell of $BaCuF_6$ material contains only 32 atoms with 4 Ba atoms, 4 Cu atoms, and 24 F atoms. The side views of both unit cells are shown in Fig 6 (a). In Table 2, we label all alkaline earth atoms and alkali elements as A, transition metal as M, and O and F elements as X. It contains the A-M, M-X and A-X bond lengths in Å. It is clear that both M and A atoms have relatively stronger interactions with X atoms due to lower bond lengths compared to the M-A bonds. The M-X distances are considerably shorter than the other two bond types. Figure 6 (b) shows the polyhedra in the materials. In a $BaCuF_6$ unit cell, each Ba atom bonds with 12 F atoms to form BaF_{12} cuboctahedra, while each Cu atom makes CuF_6 octahedra by making bonds with 12 F atoms. A single BaF_{12} cuboctahedron shares faces with four CuF_6 octahedra. In A_6MO_6, M atoms form MO_6 octahedra by bonding with 6 O atoms. However, each A element with 4 neighboring O atoms constructs an AO_4 rectangle where O atoms are at the corners and M atom is at the center. A single AO_4 rectangle shares its two short edges with two MO_6 octahedra. The lattice constant (a) of $BaCuF_6$ ($a = 8.1253$ Å) is the shortest, while Rb_6IrO_6 ($a = 9.2751$ Å) has the longest (see Table 2). It is clear that a of A_6MO_6 materials increases as $a[Na_6TcO_6] < a[K_6TcO_6] < a[Rb_6IrO_6]$. This can be mainly because atomic radius (R) of Alkali elements increases as $R[\text{Na}] < R[\text{K}] < R[\text{Rb}]$.

To find the magnetic ground state structure of the materials, We performed DFT-based structure optimization for ferromagnetic (FM), anti-ferromagnetic (AFM), and non-magnetic (NM) states. As shown in Fig. 7, we considered five AFM configurations, where AFM1, AFM2, and AFM3 are collinear configurations, and AFM4 and AFM5 are non-collinear configurations. Those collinear AFM configurations were considered for FCC structures by previous research works [18, 19, 20]. Figure 7 shows only the M atoms, as it allows us to show the directions of the spins conveniently. The atoms with spin-up and spin-down are indicated by red and blue, respectively. In the AFM1 configuration, all the spins at the middle M layer are arranged in the spin-down direction, while the bottom M layer has spin-up electrons. To create the AFM2 and AFM3 configurations, we used $2 \times 1 \times 1$ super-cell structures. Only the middle atoms get the opposite spin directions compared to the rest of the atoms in the same M layer in the $2 \times 1 \times 1$ structure for the AFM2 configuration. In the AFM3 configuration, two consecutive layers in a-direction have M atoms with spin-up while the other two have M atoms with spin-down. All the spins point toward the center in the AFM4 non-colinear configuration, whereas spin directions lie on the ab-plane in the AFM5 non-colinear configuration.

Table 3 contains the energy values for each FM, AFM, and NM state relative to the FM state. The NM state of all the materials poses high relative energy confirming those materials are magnetic. It is clear that the non-collinear

AFM configurations exhibit the highest energy compared to the FM state. This indicated that the non-collinear spin arrangements are not energetically favorable. $BaCuF_6$, Na_6TcO_6 and K_6TcO_6 materials have FM ground state, while Rb_6IrO_6 has AFM1 ground state. $BaCuF_6$ and Na_6TcO_6 retain a total magnetic moment of 1 μ_B per unit cell, whereas K_6TcO_6 provides 0.71 μ_B per unit cell.

The formation energy (E_{form}) of the magnetic ground state of the materials was calculated based on the following formula.

$$E_{\text{form}} = \frac{1}{N}(E_{\text{tot}} - \sum_i x_i E_i) \tag{3}$$

Here, the total energy of a unit formula is indicated by E_{tot}. Moreover, x_i is the number of atoms and E_i is the energy of the i^{th} element. The sum of x_i provides the number of atoms in a unit formula, which is 8 for $BaCuF_6$ and 13 for A_6MO_6. To calculate E_i for each species, we used the Pymatgen code to collect the most stable structure of each element. E_{form} indicates the thermodynamic stability of a material against its elements. The negative E_{form} in Table 3 reflects that all four materials are stable. It is also clear that E_{form} increases as $E_{\text{form}}[Na_6TcO_6] < E_{\text{form}}[K_6TcO_6] < E_{\text{form}}[Rb_6IrO_6]$. Moreover, the lowest E_{form} is found at $BaCuF_6$ material.

Table 2: The structural properties of the spintronics Materials. The bond lengths between A, M and X atoms and lattice constant (a) are mentioned in Å.

Material	A-M	M-X	A-X	a	Space Group
$BaCuF_6$	3.5184	1.8589	2.8779	8.1253	216
Na_6TcO_6	3.2793	1.9553	2.3471	9.2751	225
K_6TcO_6	3.6541	1.9600	2.6580	10.3352	225
Rb_6IrO_6	3.8064	1.9957	2.7800	10.7662	225

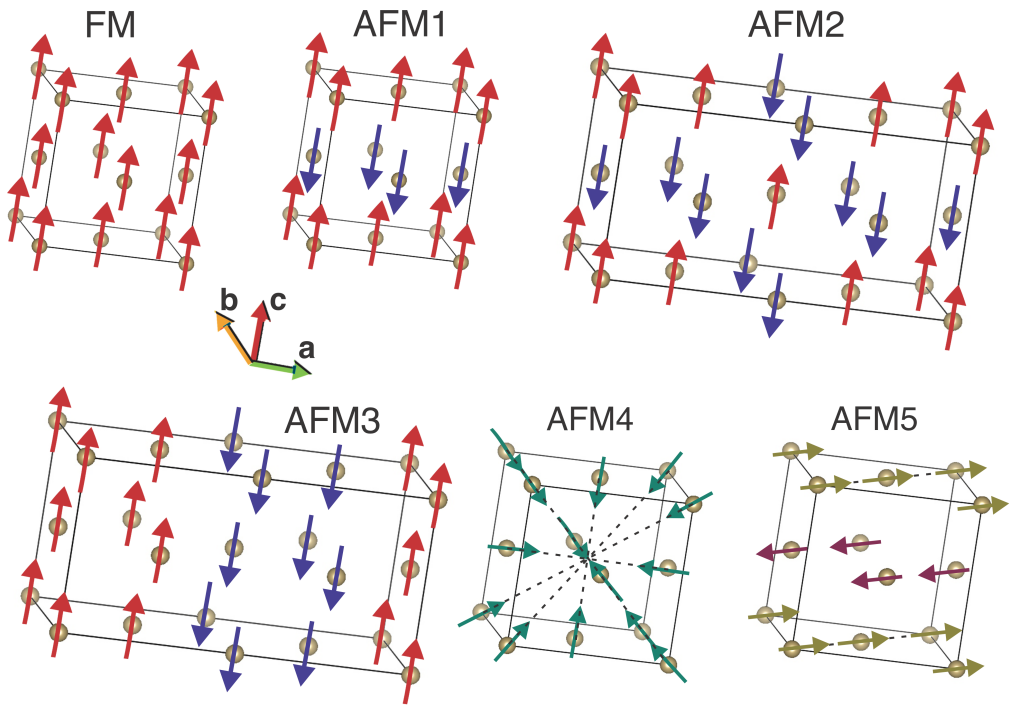

Figure 7: FM and AFM configurations. Here, only the transition metal atoms are shown.

Table 3: The energy (E) relative to FM state for NM state and each configuration of AFM phase in eV, the total magnetic moment per unit formula (magmom) in μ_B and the formation energy in eV/atom for the magnetic ground state structure based on DFT calculations. Here, negative energy of AFM state means it is stable compared to the FM state.

Material	E_{FM}	E_{NM}	E_{AFM1}	E_{AFM2}	E_{AFM3}	E_{AFM4}	E_{AFM5}	magmom (μ_B)	E_{form}
$BaCuF_6$	0.00	78.97	17.64	18.02	26.59	414.35	1157.72	1	-2.18
Na_6TcO_6	0.00	72.79	53.78	72.90	19.41	408.15	945.88	1	-1.62
K_6TcO_6	0.00	28.59	19.09	20.71	9.55	381.87	930.07	0.71	-1.57
Rb_6IrO_6	0.00	299.26	-78.63	-71.73	-63.97	221.31	407.41	0	-1.28

3.5 Mechanical Properties and Stability

Table 4: The mechanical properties of the spintronics materials. The C_{11}, C_{13} and C_{44} elastic constants, Bulk modulus (K), Shear modulus (G) and Young's modulus (Y) are mentioned in GPa. Moreover, Poisson's ratio ν is also calculated.

Material	C_{11}	C_{12}	C_{44}	K	G	Y	ν
$BaCuF_6$	36.107	35.252	12.227	35.537	4.261	12.292	0.442
Na_6TcO_6	89.134	26.645	27.420	47.474	28.891	72.056	0.247
K_6TcO_6	65.887	16.337	20.483	32.854	22.104	54.164	0.225
Rb_6IrO_6	67.104	16.342	18.462	33.045	21.023	52.035	0.238

Next, we computed the elastic constants C_{ij} $(i, j = 1, 2, 3, 4, 5, 6)$ to study the mechanical stability and properties of the materials as shown in Table 4. In crystals with cubic symmetry, $C_{11} = C_{22} = C_{33}$, $C_{12} = C_{13} = C_{23}$, and $C_{44} = C_{55} = C_{66}$. Therefore, there are only three independent elastic constants which are C_{11}, C_{12}, and C_{44}. The higher C_{11} constants of A_6MO_6 materials compared to that of $BaCuF_6$ reveal that those materials are relatively stiffer than $BaCuF_6$ in **a**, **b**, and **c** directions. Furthermore, the shear elastic constants C_{44}, C_{55} and C_{66} of A_6MO_6 materials are significantly higher than that of $BaCuF_6$. M, O, and F atoms are arranged in the materials such that M-O-M and M-F-M chains are parallel to **a**, **b**, and **c** directions in A_6MO_6 materials. M-O bonds may be stronger than M-F bonds since O atoms can contribute 2 electrons to form bonds with M atoms. In contrast, only an F atom can offer only a single electron. And also A-O-A atomic chains are also almost parallel to the **a**, **b**, and **c** directions, while A-F-A bonds make around 45° angle. Therefore, there is an extra strength from A-O bonds in those directions for A_6MO_6. This can be the main reason for having higher C_{11} constants in A_6MO_6 than in $BaCuF_6$.The Born stability criteria for the crystals with cubic unit cells are $C_{11} - C_{12} > 0$, $C_{11} + 2C_{12} > 0$ and $C_{44} > 0$. The C_{ij} constants in Table 4 proves that $BaCuF_6$ and A_6MO_6 spintronic materials are mechanically stable.

Table 4 also includes the average Bulk modulus (K), Shear modulus (G), Young's modulus (Y) and Poisson ratio (ν) which were calculated using the Hill approximation [47]. The mechanical properties were computed using the VASPKIT code [43]. It shows that the above considerable elastic constant differences affect the average mechanical properties like G and Y. Among the spintronics materials studied in this research, the highest Y can be expected from Na_6TcO_6. In contrast, the lowest Y can be expected from $BaCuF_6$. Y of $BaCuF_6$ is around 83 $\%$ lower than that of Na_6TcO_6. ν is defined as the negative ratio of the resulting transverse strain over the applied longitudinal strain in the direction of the applied force [48]. Generally, this value lies in the range of 0-0.5. Natural rubber exhibits $\nu = 0.5$ [49] and steels has $\nu = 0.3$ [50]. Rubber has a high expansion to a small axial stretching, while steel has a relatively weak expansion. Table 4 illustrates that $BaCuF_6$ value is around 0.4 while that of A_6MO_6 compounds is between $0.22 - 0.24$. This indicates that $BaCuF_6$ is more deformable elastically at a small strain. A_6MO_6 materials show lateral expansion/compression under strain is smaller than steel.

3.6 Electronic Properties

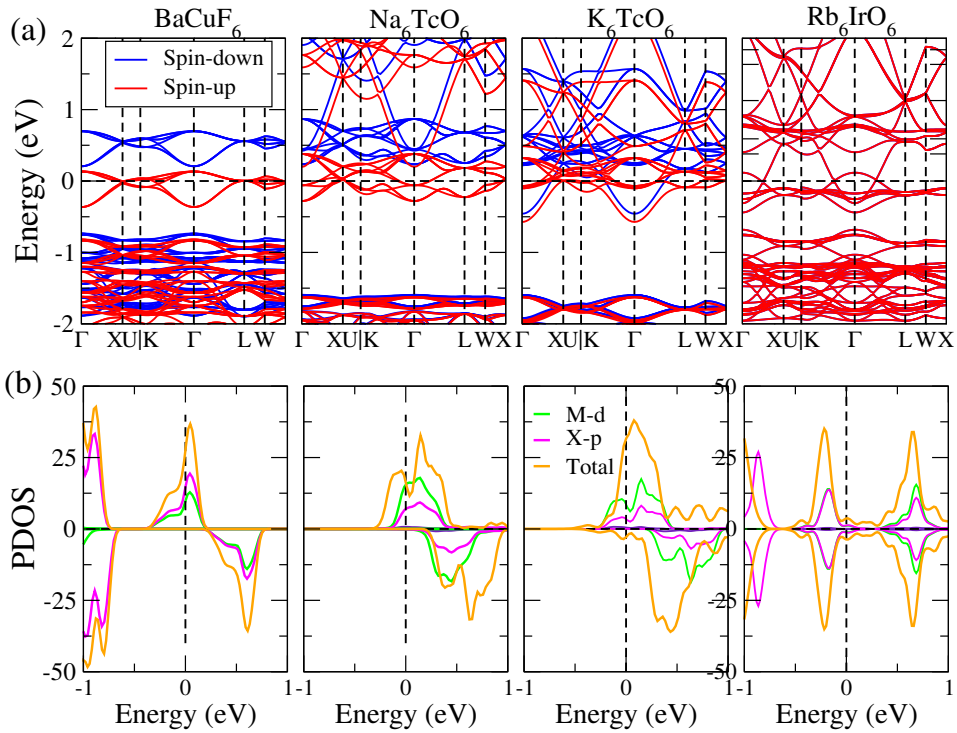

Figure 8: (a) The electronic band structures and (b) the partial density of states (PDOS) and total density of states (DOS) of the spintronics materials. Fermi energy marks zero energy. Only transition metal (M)-d and alkaline/alkali metal (A)-p orbitals contribute significantly.

Figure 8 shows the electronic band structures of the spintronics materials. Here, the spin-down bands are represented by blue lines, while red lines denote the spin-up bands. As Table 3 illustrated, only Rb_6IrO_6 is an antiferromagnetic material. All the ferromagnetic materials show spin splitting. This is more significant in $BaCuF_6$ and Na_6TcO_6 where spin-down conduction bands exist much away from the Fermi level compared to the spin-up conduction bands. As a result, those two materials exhibit half-metallic characteristics indicating only the spin-up bands can conduct. The band gap of the spin-down bands of $BaCuF_6$ is 0.94 eV. The spin-down valence bands of Na_6TcO_6 form a 1.83 eV direct band gap. In both half metals, valence band maxima and conduction band minima locate at the Γ point indicating spin-down bands act as direct band gap semiconductors. Since metallic and insulating properties depend on the spin direction, half-metals are promising materials for spin-controlled electronics and magnetism in spintronics applications. It is already used in computer memory units, and processors [51, 52].

The partial density of states (PDOS) calculations in Fig. 8 reveal that hybridization of the d-orbitals of transition metal atoms and p-orbitals of alkaline/alkali-metal atoms occurs near the Fermi level. In $BaCuF_6$, K_6TcO_6 and Na_6TcO_6 ferromagnetic materials, spin-up electrons dominate around the Fermi level. On the contrary, both spin-up and spin-down electrons contribute approximately equally in Rb_6IrO_6 antiferromagnetic material. It is also found that the contributions from p-orbitals of transition metal atoms and s-orbitals of alkaline/alkali metal atoms for PDOS near the Fermi level are negligible. The total density of states (DOS) in Fig. 8 also reveals that $BaCuF_6$ and Na_6TcO_6 are half-metals, whereas the other two materials are metals. The DOS of the spin-up energy bands of the two half-metals crosses the Fermi level, represented by the horizontal line. In contrast, the spin-down bands of these materials appear away from the Fermi level.

Table 5: The charge transfer (Δq) in electrons from Bader, Muliken, and Loewdin methods.

Material	Bader			Mulliken			Loewdin		
	Δq_{A}	Δq_{M}	Δq_{x}	Δq_{A}	Δq_{M}	Δq_{x}	Δq_{A}	Δq_{M}	Δq_{x}
$BaCuF_6$	1.75	1.66	-0.57	1.91	1.73	-0.61	1.81	1.62	-0.57
Na_6TcO_6	0.83	2.32	-1.22	0.73	1.81	-1.03	0.70	1.72	-0.98
K_6TcO_6	0.76	2.07	-1.11	0.76	1.80	-1.06	0.76	1.70	-1.04
Rb_6IrO_6	0.79	2.34	-1.18	0.81	1.97	-1.13	0.81	1.88	-1.12

Table 5 shows the charge transfer (Δq) of each atomic species of the spintronics materials calculated using Bader, Mulliken, and Loewdin techniques. The Bader charge analysis was performed using the algorithm developed by Tang et. al [53], Sanville et. al [54] and Henkelman et. al [55], while Mulliken and Loewdin population analysis were carried out by employing the LOBSTER code [56]. There are small differences in the charge transfers calculated from different methods. However, based on all three techniques in Table 5, the A and M atoms lose electrons, although O and F atoms gain electrons. Therefore, A-X and M-X bond lengths have ionic character. The O atoms draw more than one electron as they can acquire up to two. In contrast, the F atoms acquire less than one electron. It evidences that the alkali metal elements are in their usual oxidization state, $+1$. At the same time, the Ba has its common oxidization state ($+2$) as Ba is an alkaline earth metal. The transition metal element Tc of Na_6TcO_6 material have an oxidization state between $+2$ and $+3$, whereas that of K_6TcO_6 is $+2$. The oxidization state of Ir in Rb_6IrO_6 is also between $+2$ and $+3$. Cu atoms of $BaCuF_6$ have an oxidization state between $+1$ and $+2$. As described before, MO_6 octahedra and AO_4 rectangles are in A_6MO_6, and CuF_6 octahedra and BaF_{12} cuboctahedra are in $BaCuF_6$. Based on the data in Table 5, it can be shown that A_6MO_6 materials contain MO_6^{5-} and AO_4^{4-} complexes, while $BaCuF_6$ has CuF_6^{2-} and BaF_{12}^{5-} complexes.

3.7 Thermodynamic Properties and Dynamical Stability

Next, we investigated the thermodynamic properties of the spintronics materials based on the following expressions.

$$\theta_D = \frac{h}{k_B}\left(\frac{3N}{4\pi V_0}\right)^{\frac{1}{3}} \nu_D \tag{4}$$

$$\nu_D = \left[\frac{1}{3}\left(\frac{2}{\nu_l^3} + \frac{1}{\nu_t^3}\right)\right]^{-\frac{1}{3}} \tag{5}$$

$$\nu_l = \left(\frac{3K+4G}{3\rho}\right)^{\frac{1}{2}} \text{ and } \nu_t = \left(\frac{G}{\rho}\right)^{\frac{1}{2}} \tag{6}$$

Here, θ_D is the Debye temperature which can be computed using Debye sound velocity (ν_D) as shown in Eq. 4. In this expression, N, V_0, and ρ are the number of atoms, volume, and density of the unitcell, respectively. Moreover, h represents Plank's constant, and k_B indicates Boltzmann's constant. ν_D depends on the longitudinal (ν_l) and transverse (ν_t) sound velocities as explained by Eq.5[57]. ν_l and ν_t velocity components can be determined based on the K and G mechanical properties mentioned in Table 4. According to Eq. 4, 5 and 6 illustrate that θ_D increases if the K and G mechanical properties increase.

We studied C_v against temperature T employing the Phonopy code [44]. In this code, C_v is calculated based on the following formula,

$$C_v = \sum_{\mathbf{q}j} k_B \left(\frac{\hbar\omega_{\mathbf{q}j}}{k_B T}\right)^2 \frac{\exp(\hbar\omega_{\mathbf{q}j}/k_B T)}{[\exp(\hbar\omega_{\mathbf{q}j}/k_B T) - 1]^2}\ , \tag{7}$$

where each phonon frequency of $\mathbf{q}$ wave vector at jth phonon band index is indicated by $\omega_{\mathbf{q}j}$ and $\hbar$ is the reduced Plank's constant [44]. Table 6 The G values of A_6MO_6 materials are significantly higher than that of $BaCuF_6$. Thus, this can be the main reason for having considerably lower θ_D in $BaCuF_6$ compared to the other three materials. It is clear from Fig. 9 that the C_{v} of $BaCuF_6$ is much smaller than that of the A_6MO_6 materials. The C_{v} of $BaCuF_6$ is 176.15 $\mathrm{JK^{-1}mol^{-1}}$, whereas $C_{\mathrm{v}} > 1100$ $\mathrm{JK^{-1}mol^{-1}}$ for A_6MO_6 materials at 300 K temperature. We also investigated the phonon dispersion of the spintronic materials as shown in Fig. 10. It evidences that those materials are dynamically stable at 0 K temperature as there are no imaginary frequencies in the plots.

Table 6: The thermodynamic properties of the Spintronic materials. The density (ρ), longitudinal (v_{l}), transverse (v_{t}) and average (v_{D}) sound velocities, Debye temperature (θ_{D}) and the specific heat capacity at 300 K ($C_{\mathrm{v}}^{300\mathrm{K}}$) are mentioned.

Material	ρ (gcm^{-3})	v_{l} (ms^{-1})	v_{t} (ms^{-1})	v_{D} (ms^{-1})	θ_{D} (K)	$C_{\mathrm{v}}^{300\mathrm{K}}$ (JK^{-1}mol^{-1})
BaCuF6	0.97	6,503.12	2,090.90	2,951.59	216.30	176.15
Na6TcO6	0.69	11,157.54	6,467.14	8,358.68	630.87	1110.31
K6TcO6	0.64	9,832.71	5,855.63	7,509.42	508.64	1147.89
Rb6IrO6	0.45	11,627.59	6,821.87	8,786.82	571.34	1152.78

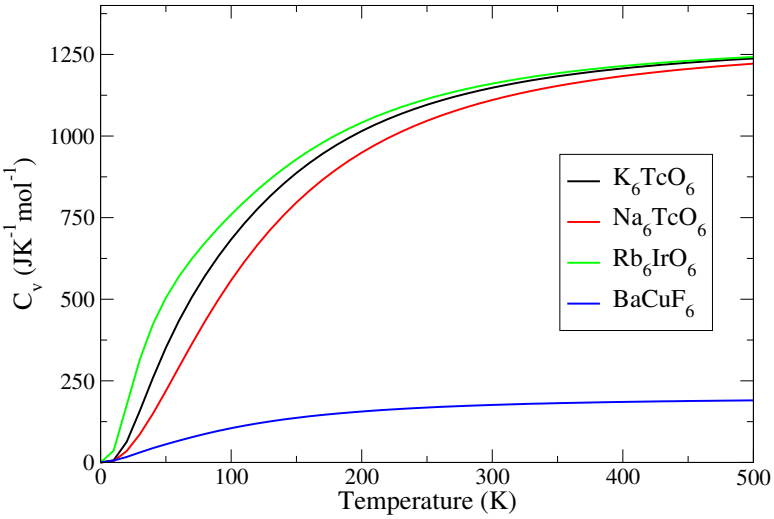

Figure 9: The specific heat capacity (C_v) of the spintronic materials as a function of temperature (T).

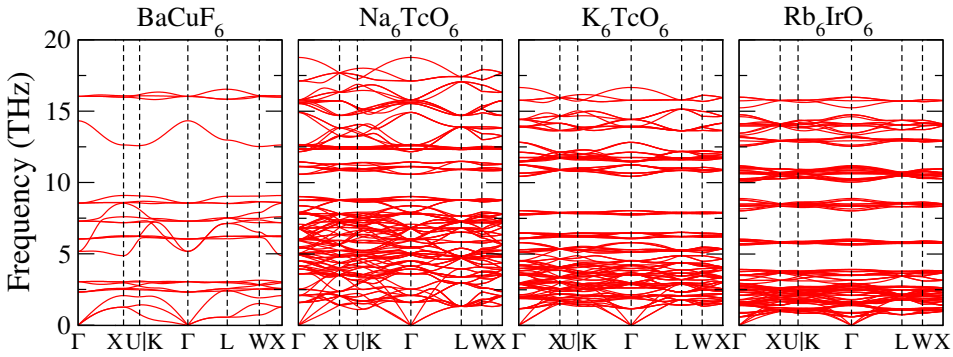

Figure 10: Phonon dispersion of the spintronic materials. Absence of negative frequencies implies that the materials are dynamically stable.

4 Conclusion

DFT based screening approaches for discovering materials have been widely used in materials science, which, however, is not suitable for finding new magnetic materials as it consumes too much computational resources: finding the magnetic ground state of a single magnetic material is much more computationally demanding due to it has multiple antiferromagnetic configurations. Here, we developed a computational framework to de novo design novel spintronic materials by combining GAN, machine learning classifiers, and DFT. We first studied the chemical space to find the most probable combination of elements for transition metal elements-based magnetic materials. We found that ternary transition metal-based oxides and fluorides are most likely to have a magnetic ground state. Next, we developed the deep neural network(DNN) and Random forest classifier models to screen candidate magnetic materials out of

the CubicGAN-generated ternary structures. Both models achieve accuracies around 90%, while DNN shows less over-training. Thus, the DNN model can work well for screening new magnetic materials. Out of 141 ternary materials generated by CubicGAN, 45 were classified by our DNN model as magnetic materials. Our DFT studies discovered that three transition metal-based oxides and one fluoride were stable magnetic compounds. Furthermore, we considered NM, FM, three AFM collinear (AFM1, AFM2, and AFM3), and two AFM noncollinear (AFM4 and AFM5) configurations to find the minimum energy states. We found that Na_6TcO_6, K_6TcO_6, and $BaCuF_6$ are ferromagnetic compounds while Rb_6IrO_6 is an antiferromagnetic material with AFM1 configuration. Na_6TcO_6 and $BaCuF_6$ are half metals where only spin-up bands contribute to electron conduction. Moreover, A_6MO_6 materials hold higher thermal capacity (C_v) than that in $BaCuF_6$. At 300 K temperature, $C_v \approx 1100$ JK^{-1} mol^{-1} for A_6MO_6 materials, whereas $C_v \approx 176$ JK^{-1} mol^{-1} for $BaCuF_6$. Our work demonstrates the significant potential of the new generation of deep learning and machine learning-based generative design frameworks in discovering novel functional materials. As for future work, GAN models can be developed to generate potential spintronic materials with all types of space group symmetries. Focusing on fluoride and oxide ternary materials can enhance efficiency, as they have a high probability of being magnetic materials. In the future, binary and quaternary materials can also be studied to generate new spintronic materials.

5 Data Availability

The structures of the materials generated from CubicGAN model can be downloaded from Carolina Materials Database at http://www.carolinamatdb.org/. The crystallographic information files (CIF) of the stable structures are included in the Supporting Information.

6 Code Availability

The source code of the classifier can be obtained from github at https://github.com/dilangaem/SpinAI.

7 Acknowledgement

The research reported in this work was supported in part by National Science Foundation under the grant and 1940099, 1905775, and 2110033. The views, perspectives, and content do not necessarily represent the official views of the NSF.

8 Author Contributions

Conceptualization, E.S.; methodology, E.S.,Y.Z.; software, E.S.,Y.Z., and J.H.; resources, J.H.; writing–original draft preparation, E.S., and Y.Z.; writing–review and editing, J.H, and E.S.; visualization, E.S. and Y.Z.; supervision, J.H.; funding acquisition, J.H.

9 Competing Interests

The authors declare no competing interests.

References

[1] Jorge Puebla, Junyeon Kim, Kouta Kondou, and Yoshichika Otani. Spintronic devices for energy-efficient data storage and energy harvesting. *Communications Materials*, 1(1), May 2020.

[2] Soubantika Palchoudhury, Karthik Ramasamy, and Arunava Gupta. Recent progress in spintronic materials. *Material Matters*, pages 97–103, 12 2016.

[3] Jagadeesh S. Moodera and Patrick LeClair. A quantum leap. *Nature News*, page 707–708, 2003.

[4] Inga Ennen, Daniel Kappe, Thomas Rempel, Claudia Glenske, and Andreas Hütten. Giant magnetoresistance: Basic concepts, microstructure, magnetic interactions and applications, Jun 2016.

[5] H.A.M. van den Berg, U. Hartmann, R. Coehoorn, M.A.M. Gijs, P. Grünberg, T. Rasing, and K. Röll. *Magnetic Multilayers and Giant Magnetoresistance: Fundamentals and Industrial Applications*. Springer Series in Surface Sciences. Springer Berlin Heidelberg, 2013.

[6] V. Baltz, A. Manchon, M. Tsoi, T. Moriyama, T. Ono, and Y. Tserkovnyak. Antiferromagnetic spintronics. *Rev. Mod. Phys.*, 90:015005, Feb 2018.

[7] Ding-Fu Shao, Shu-Hui Zhang, Ming Li, Chang-Beom Eom, and Evgeny Y. Tsymbal. Spin-neutral currents for spintronics. *Nature News*, Dec 2021.

[8] Sergey A. Adonin, Igor D. Gorokh, Pavel A. Abramov, Alexander S. Novikov, Ilya V. Korolkov, Maxim N. Sokolov, and Vladimir P. Fedin. Chlorobismuthates trapping dibromine: Formation of two-dimensional supramolecular polyhalide networks with br2 linkers. *European Journal of Inorganic Chemistry*, 2017(42):4925–4929, 2017.

[9] Sergey A. Adonin, Igor D. Gorokh, Denis G. Samsonenko, Alexander S. Novikov, Ilya V. Korolkov, Pavel E. Plyusnin, Maxim N. Sokolov, and Vladimir P. Fedin. Binuclear and polymeric bromobismuthate complexes: Crystal structures and thermal stability. *Polyhedron*, 159:318–322, 2019.

[10] Andrey N. Usoltsev, Nikita A. Korobeynikov, Alexander S. Novikov, Pavel E. Plyusnin, Boris A. Kolesov, Vladimir P. Fedin, Maxim N. Sokolov, and Sergey A. Adonin. One-dimensional diiodine–iodobismuthate(iii) hybrids cat3[Bi2I9](I2)3: Syntheses, stability, and optical properties. *Inorganic Chemistry*, 59(23):17320–17325, 2020. PMID: 33202124.

[11] Chen Shen, Qiang Gao, Nuno M. Fortunato, Harish K. Singh, Ingo Opahle, Oliver Gutfleisch, and Hongbin Zhang. Designing of magnetic mab phases for energy applications. *J. Mater. Chem. A*, 9:8805–8813, 2021.

[12] Muhammad Salman Khan, Banat Gul, Gulzar Khan, Benabdellah Ghlamallah, Shaukat Ali Khattak, Majid Khan, Tahirzeb Khan, Muhammad Ajaz, Syed Zulfiqar, and Wazir Muhammad. Insight into the electronic, optical and transport nature of al2cdx4 (x = s, se and te) employing the accurate mbj approach: Novel materials for opto-electronic devices. *Materials Science in Semiconductor Processing*, 135:106098, 2021.

[13] Yiyuan Wu, Chao Ren, and Qianglin Wei. Novel ternary compound transition metal dichalcogenide tinbs4 as promising anodes materials for li-ion batteries: A dft study. *Applied Surface Science*, 615:156322, 2023.

[14] Xiaojun Zhao, Peng Wang, Erfei Lv, Chongchong Wu, Kai Ma, Zhengyang Gao, Ian D. Gates, and Weijie Yang. Screening mxenes for novel anode material of lithium-ion batteries with high capacity and stability: A dft calculation. *Applied Surface Science*, 569:151050, 2021.

[15] Chengxi Huang, Junsheng Feng, Fang Wu, Dildar Ahmed, Bing Huang, Hongjun Xiang, Kaiming Deng, and Erjun Kan. Toward intrinsic room-temperature ferromagnetism in two-dimensional semiconductors. *Journal of the American Chemical Society*, 140(36):11519–11525, August 2018.

[16] Zhou Jiang, Peng Wang, Xue Jiang, and Jijun Zhao. MBene (MnB): a new type of 2d metallic ferromagnet with high curie temperature. *Nanoscale Horizons*, 3(3):335–341, 2018.

[17] Weiwei Sun, Yu Xie, and Paul R. C. Kent. Double transition metal MXenes with wide band gaps and novel magnetic properties. *Nanoscale*, 10(25):11962–11968, 2018.

[18] Ya. M. Ridnyi, A. A. Mirzoev, and D. A. Mirzaev. Ab initio simulation of dissolution energy and carbon activity in fcc fe. *Physics of the Solid State*, 59(7):1279–1284, July 2017.

[19] T Chatterji, L P Regnault, S Ghosh, and A Singh. Magnetic excitations in frustrated fcc type-III antiferromagnet mns2. *Journal of Physics: Condensed Matter*, 31(12):125802, January 2019.

[20] Liu Pan, Zhen Wang, Qingqing Wang, Zhixiao Liu, Min Pan, Zheng Huang, and Lu Wu. Influence of th, zr, and ti dopants on solution property of xe in uranium dioxide with defects: A DFT + u study. *Metals*, 12(5):879, May 2022.

[21] Weiyi Xia, Masahiro Sakurai, Balamurugan Balasubramanian, Timothy Liao, Renhai Wang, Chao Zhang, Huaijun Sun, Kai-Ming Ho, James R. Chelikowsky, David J. Sellmyer, and Cai-Zhuang Wang. Accelerating the discovery of novel magnetic materials using machine learning–guided adaptive feedback. *Proceedings of the National Academy of Sciences*, 119, 11 2022.

[22] Teng Long, Nuno M. Fortunato, Yixuan Zhang, Oliver Gutfleisch, and Hongbin Zhang. An accelerating approach of designing ferromagnetic materials via machine learning modeling of magnetic ground state and curie temperature. *Materials Research Letters*, 9:169–174, 01 2021.

[23] Shuaihua Lu, Qionghua Zhou, Yilv Guo, and Jinlan Wang. On-the-fly interpretable machine learning for rapid discovery of two-dimensional ferromagnets with high curie temperature. *Chem*, 8, 12 2021.

[24] Yong Zhao, Mohammed Al-Fahdi, Ming Hu, Edirisuriya MD Siriwardane, Yuqi Song, Alireza Nasiri, and Jianjun Hu. High-throughput discovery of novel cubic crystal materials using deep generative neural networks. *Advanced Science*, 8(20):2100566, 2021.

[25] Juhwan Noh, Jaehoon Kim, Helge S Stein, Benjamin Sanchez-Lengeling, John M Gregoire, Alan Aspuru-Guzik, and Yousung Jung. Inverse design of solid-state materials via a continuous representation. *Matter*, 1(5):1370–1384, 2019.

[26] Tian Xie, Xiang Fu, Octavian-Eugen Ganea, Regina Barzilay, and Tommi Jaakkola. Crystal diffusion variational autoencoder for periodic material generation. *arXiv preprint arXiv:2110.06197*, 2021.

[27] Callum J Court, Batuhan Yildirim, Apoorv Jain, and Jacqueline M Cole. 3-d inorganic crystal structure generation and property prediction via representation learning. *J. Chem. Inf. Model.*, 60(10):4518–4535, 2020.

[28] Yong Zhao, Edirisuriya M Dilanga Siriwardane, Zhenyao Wu, Ming Hu, Nihang Fu, and Jianjun Hu. Physics guided generative adversarial networks for generations of crystal materials with symmetry constraints. *arXiv preprint arXiv:2203.14352*, 2022.

[29] Zekun Ren, Juhwan Noh, Siyu Tian, Felipe Oviedo, Guangzong Xing, Qiaohao Liang, Armin Aberle, Yi Liu, Qianxiao Li, Senthilnath Jayavelu, et al. Inverse design of crystals using generalized invertible crystallographic representation. *arXiv preprint arXiv:2005.07609*, 2020.

[30] Scott Kirklin, James E Saal, Bryce Meredig, Alex Thompson, Jeff W Doak, Muratahan Aykol, Stephan Rühl, and Chris Wolverton. The open quantum materials database (oqmd): assessing the accuracy of dft formation energies. *npj Computational Materials*, 1(1):1–15, 2015.

[31] Ian Goodfellow et al. Generative adversarial nets. *Adv. Neural Inf. Process. Syst.*, 27, 2014.

[32] Ishaan Gulrajani, Faruk Ahmed, Martin Arjovsky, Vincent Dumoulin, and Aaron Courville. Improved training of wasserstein gans. *arXiv preprint arXiv:1704.00028*, 2017.

[33] François Chollet et al. Keras. `https://keras.io`, 2015.

[34] Martín Abadi, Ashish Agarwal, Paul Barham, Eugene Brevdo, Zhifeng Chen, Craig Citro, Greg S. Corrado, Andy Davis, Jeffrey Dean, Matthieu Devin, Sanjay Ghemawat, Ian Goodfellow, Andrew Harp, Geoffrey Irving, Michael Isard, Yangqing Jia, Rafal Jozefowicz, Lukasz Kaiser, Manjunath Kudlur, Josh Levenberg, Dandelion Mané, Rajat Monga, Sherry Moore, Derek Murray, Chris Olah, Mike Schuster, Jonathon Shlens, Benoit Steiner, Ilya Sutskever, Kunal Talwar, Paul Tucker, Vincent Vanhoucke, Vijay Vasudevan, Fernanda Viégas, Oriol Vinyals, Pete Warden, Martin Wattenberg, Martin Wicke, Yuan Yu, and Xiaoqiang Zheng. TensorFlow: Large-scale machine learning on heterogeneous systems, 2015. Software available from tensorflow.org.

[35] F. Pedregosa, G. Varoquaux, A. Gramfort, V. Michel, B. Thirion, O. Grisel, M. Blondel, P. Prettenhofer, R. Weiss, V. Dubourg, J. Vanderplas, A. Passos, D. Cournapeau, M. Brucher, M. Perrot, and E. Duchesnay. Scikit-learn: Machine learning in Python. *Journal of Machine Learning Research*, 12:2825–2830, 2011.

[36] G. Kresse and J. Hafner. ab initio. *Phys. Rev. B*, 47:558–561, Jan 1993.

[37] G. Kresse and J. Hafner. ab initio. *Phys. Rev. B*, 49:14251–14269, May 1994.

[38] J. Furthmüller G. Kresse. Efficiency of ab initio total energy calculations for metals and semiconductors using a plane-wave basis set. *Comput. Mater. Sci.*, 6:15–50, jul 1996.

[39] G. Kresse and J. Furthmüller. Efficient iterative schemes for ab initio total-energy calculations using a plane-wave basis set. *Phys. Rev. B*, 54:11169–11186, Oct 1996.

[40] John P. Perdew, Kieron Burke, and Matthias Ernzerhof. Generalized gradient approximation made simple. *Phys. Rev. Lett.*, 77:3865–3868, Oct 1996.

[41] John P. Perdew, Kieron Burke, and Matthias Ernzerhof. Generalized gradient approximation made simple [phys. rev. lett. 77, 3865 (1996)]. *Phys. Rev. Lett.*, 78:1396–1396, Feb 1997.

[42] Stefano Baroni, Stefano de Gironcoli, Andrea Dal Corso, and Paolo Giannozzi. Phonons and related crystal properties from density-functional perturbation theory. *Rev. Mod. Phys.*, 73:515–562, Jul 2001.

[43] Vei Wang, Nan Xu, Jin-Cheng Liu, Gang Tang, and Wen-Tong Geng. Vaspkit: A user-friendly interface facilitating high-throughput computing and analysis using vasp code. *Computer Physics Communications*, 267:108033, Oct 2021.

[44] A Togo and I Tanaka. First principles phonon calculations in materials science. *Scr. Mater.*, 108:1–5, Nov 2015.

[45] Vladimir I. Anisimov, Jan Zaanen, and Ole K. Andersen. Band theory and mott insulators: Hubbard u instead of stoner i. *Phys. Rev. B*, 44:943–954, Jul 1991.

[46] A Rohrbach, J Hafner, and G Kresse. Electronic correlation effects in transition-metal sulfides. *Journal of Physics: Condensed Matter*, 15(6):979, feb 2003.

[47] Richard Hill. The elastic behaviour of a crystalline aggregate. *Proceedings of the Physical Society. Section A*, 65(5):349, 1952.

[48] B.K.O. Cheung and J.P. Carey. 6 - micromechanics for braided composites. In Jason P. Carey, editor, *Handbook of Advances in Braided Composite Materials*, pages 239–257. Woodhead Publishing, 2017.

[49] Dominick Rosato and Donald Rosato. 3 - design parameter. In Dominick Rosato and Donald Rosato, editors, *Plastics Engineered Product Design*, pages 161–197. Elsevier Science, Amsterdam, 2003.

[50] Yuriy M. Poplavko. Chapter 2 - mechanical properties of solids. In Yuriy M. Poplavko, editor, *Electronic Materials*, pages 71–93. Elsevier, 2019.

[51] David D. Awschalom and James M. Kikkawa. Electron spin and optical coherence in semiconductors. *Physics Today*, 52(6):33–38, 1999.

[52] Warren E. Pickett and Jagadeesh S. Moodera. Half metallic magnets. *Physics Today*, 54(5):39–44, 2001.

[53] W Tang, E Sanville, and G Henkelman. A grid-based bader analysis algorithm without lattice bias. *Journal of Physics: Condensed Matter*, 21(8):084204, jan 2009.

[54] Edward Sanville, Steven D. Kenny, Roger Smith, and Graeme Henkelman. Improved grid-based algorithm for bader charge allocation. *Journal of Computational Chemistry*, 28(5):899–908, 2007.

[55] Graeme Henkelman, Andri Arnaldsson, and Hannes Jónsson. A fast and robust algorithm for bader decomposition of charge density. *Computational Materials Science*, 36(3):354–360, 2006.

[56] Christina Ertural, Simon Steinberg, and Richard Dronskowski. Development of a robust tool to extract mulliken and löwdin charges from plane waves and its application to solid-state materials. *RSC Adv.*, 9:29821–29830, 2019.

[57] C. Li and Z. Wang. 9 - computational modelling and ab initio calculations in max phases – i. In I.M. Low, editor, *Advances in Science and Technology of Mn+1AXn Phases*, pages 197–222. Woodhead Publishing, 2012.